ISSN 1063-7834, Physics of the Solid State, 2020, Vol. 62, No. 3, pp. 389–400. © Pleiades Publishing, Ltd., 2020.
Russian Text © The Author(s), 2020, published in Fizika Tverdogo Tela, 2020, Vol. 62, No. 3, pp. 339–350.

METALS

Experimental and Theoretical Study of the Atomic Structure Evolution of High-Entropy Alloys Based on Fe, Cr, Ni, Mn, and Co upon Thermal and Radiation Aging

E. A. Meshkov[a, b, *], I. I. Novoselov[a, b], A. V. Yanilkin[a, b], S. V. Rogozhkin[c, d], A. A. Nikitin[c, d], A. A. Khomich[c], A. S. Shutov[c], B. A. Tarasov[d], S. E. Danilov[e], and V. L. Arbuzov[e]

[a] *Moscow Institute of Physics and Technology, Dolgoprudny, Russia*
[b] *Dukhov All-Russian Scientific Research Institute of Automation, Moscow, Russia*
[c] *Alikhanov Institute of Theoretical and Experimental Physics, SRC Kurchatov Institute, Moscow, Russia*
[d] *National Research Nuclear University MEPhI, Moscow, Russia*
[e] *Mikheev Institute of Metal Physics, Ural Branch, Russian Academy of Sciences, Yekaterinburg, Russia*
**e-mail: meshkov@phystech.edu*

Received March 26, 2019; revised October 21, 2019; accepted October 21, 2019

Abstract—A comprehensive experimental–theoretical study of the processes of local ordering of multicomponent alloys has been carried out. Atom probe tomography and measurement of electrical resistance during isochronal annealing are used as experimental techniques. Atomistic modeling methods and the multiscale paradigm based on quantum mechanical calculations were used in the theoretical study. The experimental and theoretical approach used made it possible for the first time to detect the initial stage of decomposition of a CoCrFeNi alloy solid solution with the formation of Ni_4Cr and Ni_2Cr precipitates.

Keywords: high-entropy alloys, first-principle calculations, Monte Carlo, atom-probe tomography, electrical resistance

DOI: 10.1134/S1063783420030130

1. INTRODUCTION

The first results on multicomponent equiatomic metal alloys were obtained in 2004 by Yeh [1] and Cantor [2]. In these works, such alloys were shown to be capable to form solid solutions with highly symmetric crystal lattices (cubic face-centered (fcc) or body-centered (bcc)). According to generally accepted formulation, this class of materials involves alloys containing no less than four basic elements with concentrations ranging from 5 to 35 at %. Due to the large configuration entropy arising in such alloys compared to traditional alloys, this class of compounds is called high-entropy alloys (HEAs). Nevertheless, it was shown [3–6] that configuration entropy is not always the main factor that determines the phase composition of HEAs. Other factors should also be accounted for, for example, the enthalpies of mixing of the components, the contributions of the vibrational and electronic entropies, etc. Several techniques were proposed to forecast the phase composition of HEAs [7–14]. In these works, various numerical criteria of forming a disordered solid solution or the secondary phase precipitates were proposed. These criteria are based on the enthalpies of formation of binary compounds [7], enthalpies of formation [8] and the Gibbs energies [11] of intermetallides and a disordered solid solution, configuration and excess entropy [9], interatomic distances and bulk elasticity moduli [10]. The differences in the band structure [12], electronegativity [13], enthalpies of mixing, and atomic radii [14] are also used. Nevertheless, none of these approaches is able to determine the exact structures and phase compositions of HEAs. Interest in HEAs is growing rapidly due to the unique properties of some of the alloys studied [4]. For example, the Cantor CoCrFeMnNi equiatomic alloy exhibits an excellent combination of mechanical properties, such as ultimate ductility [15, 16], high tensile strength [17, 18], hardness [19], and high resistance to destruction at cryogenic temperatures [16, 18]. The MoNbTaVW alloy from refractory metals demonstrates high heat resistance [20]. The $Al_{0.5}CoCrCuFeNi$ alloy has high fatigue resistance [21], and both CoCrFeNiTi and AlCoCrFeNiTi have excellent wear resistance [22]. The Cantor alloy and similar HEAs were also shown to have high resistance to radiation-induced degradation processes, such as swelling [23, 24], hardening [24, 25] and segregation [26]. The CoCrFeNi alloys (CCFN) are among the most studied HEAs. The phase composition of CCFN was studied using X-ray diffraction (XRD) [27],

energy dispersive X-ray method (EDX) [28], neutron diffraction [29] and high-angle dark-field transmission microscopy (HAADF) [30]. Most studies showed that CCFN forms a single-phase solid solution [14, 27, 31, 32]. However, there is some experimental evidence of a more complex phase composition of CCFN. For example, high-energy XRD analysis showed the presence of two fcc sublattices with close values of lattice parameters [29]. Moreover, HAADF and EDX studies showed the formation of precipitates [28] and local ordering of Cr atoms [30]. Also, the formation of Cr-saturated precipitates with bcc and tetragonal lattice structure was found in [33]. In [34], it was shown that σ phase, an ordered B_2 phase, and $M_{23}C_6$ carbides are formed in CoCrFeMnNi alloy at temperatures up to 1000 K, 1200 K, and 1400 K, respectively. The B_2 phase with a bcc lattice containing nickel and aluminum was found after plastic deformation [35].

The CCFN alloy was also intensively investigated using numerous theoretical approaches, such as thermodynamic calculations [3, 36], classical molecular dynamics (MD) [37, 38], electron density functional theory (DFT) [7, 30, 39], quantum MD (QMD) [40, 41] and atomistic DFT-based Monte Carlo calculations (AIMC) [42]. The main disadvantage of thermodynamic calculations is the low accuracy, while the MD, QMD, and AIMC are typically characterized by small temporal and spatial scales. As a consequence, the results obtained by these methods often have insufficient reliability. In this work, we carry out a comprehensive experimental–theoretical investigation of local ordering in CCFN using such experimental methods as atom-probe tomography and electrical resistence measurements upon thermal aging of the initial and irradiated HEA samples. As was shown many times [43, 44], the change in electrical resistance correlates with structural changes in multicomponent alloys. Upon reaching temperatures sufficient for the state of equilibrium to be established upon diffusion, the electric resistance follows the equilibrium dependence with the change in temperature [45]. The use of radiation to speed up diffusion processes makes it possible to detect the changes in the structure at lower temperatures [46, 47]. The theoretical part of the study is carried out by means of atomistic Monte Carlo using potential [48]. This approach makes it possible to carry out calculations on experimentally achievable temporal and spatial scales with an accuracy close to the DFT accuracy.

The paper is organized as follows. In Subsections 2.1 and 2.2, we describe the experimental and theoretical methods to be used. In Subsection 3.1, the experimental results of atom-probe tomography of the initial CoCrFeNiMn alloy are given. In Subsection 3.2, the results of electric resistance measurements under isochronal annealing at temperatures ranging from 300 to 900 K for CoCrFeNiMn, CoCrFeNi, and CrFeNiMn samples are described. And finally, in Subsection 3.3, the results of a theoretical study of the CoCrFeNi alloy are presented.

2. RESEARCH METHODS

In this work, a comprehensive theoretical–experimental study of the atomic evolution of CoCrFeNi, CoCrFeNiMn, and CrFeNiMn structures during thermal and radiation aging was carried out. The combined approach allows us to obtain the most complete information about the object of study, to facilitate verification of experimental data, as well as theoretical results.

2.1. Experimental Methods

The experimental part of the work involves the fabrication and characterization of the HEA samples, as well as the measurements of the curves of isochronal annealing of electrical resistance in the initial state and after electron irradiation. Samples of all three compositions were manufactured using similar techniques, the same equipment and starting materials. The atom probe tomography (APT) method was used to characterize the state of the obtained samples. Due to the high cost and labor expenses of APT, only CoCrFeNiMn alloy was investigated by this method, since it has the most complex chemical composition. To study the atomic structure evolution of HEAs, the dependences of the relative change in resistance on temperature were measured (the so-called curves of isochronal annealing) for samples in the initial state and after electronic exposure. Details of each stage of the experimental part of the work are described in the following subsections.

2.1.1. Samples fabrication. Samples of high-entropy alloys were made from pure elements (high-purity iron, electrolytic nickel and cobalt remelted in vacuum, electrolytic chromium and manganese were preremelted in an arc furnaces for cleaning) by arc melting with a nonconsumable tungsten electrode in an argon atmosphere, purified by preliminary remelting of a zirconium getter. 60 g equiatomic alloy ingots were turned over and remelted at least 7 times to increase homogeneity. The obtained ingots were forged into rectangular tiles and annealed for 3 h in an argon atmosphere at a temperature of 1000°C for homogenization of a solid solution. To prevent the evaporation of manganese, the alloys were wrapped into molybdenum foil. After annealing, an outer 0.5 mm thick layer was removed from the samples and the material was subjected to cold rolling into tapes of various thicknesses. Samples for investigations were made from the obtained tapes and annealed in vacuum for 0.5 h at a temperature of 800°C to remove stresses and for recrystallization.

2.1.2. Characterization of the original structure. To study the initial structure of the samples, the analysis of atomic-scale distributions of chemical elements in

the studied alloys was carried out. For this purpose, a PAZL-3D (IT-EF) setup for atom-probe tomography was used [49]. During research, the samples temperature was about 50 K. The data were collected at a constant voltage of 1 to 9 kV on the samples and a laser pulse duration of 300 fs, a frequency of laser pulses of 25 kHz, a pulse energy of 0.1–5 mJ, and a wavelength of 515 nm of the laser radiation harmonic. During the study, the vacuum was kept at the level of (5–7) × 10^{-10} Torr, and evaporation rate was ~5 atoms per 1000 laser impacts.

To analyze the local homogeneity of the solution and the degree of short-range order, we used the "local chemical enrichment method." The general principles of application of this method are described in [50]. This method allows one to analyze a complete set of atomic-probe data for the presence or absence of the regions corresponding to the initial stages of nucleation of secondary phases. The essence of the algorithm is to find the distribution of concentrations of chemical elements in the spherical regions around atoms of a selected type. In this case, the frequency distribution of concentrations of various components is plotted in a sphere containing the nearest neighbors. Then, the obtained frequency distribution is analyzed in comparison with the binomial distribution corresponding to a random arrangement of atoms in the material. Deviation of the frequency distribution from binomial indicates the decay of a disordered solid solution.

2.1.3. Measuring the temperature dependence of electric resistance. To measure the residual electrical resistance in liquid helium, a V2-39 nanovoltmeter and a P320 current stabilizer were used. The measurements were carried out using the standard four-contact method with an error of 0.02%. In order to avoid distortion of the results associated with the contacts, the samples in the form of a foil with a thickness of about 200 μm were supplied with potential contacts of the same material. The uniformity of irradiation along the depth of the samples was due to the fact that electron ranges exceed the thickness of the samples by more than an order of magnitude. Isochronal annealing was carried out in an oven mounted on a STG-40 Dewar transport vessel in a helium atmosphere purified by a titanium getter. The oxygen concentration was no higher than 10^{-10}%. The accuracy of temperature maintenance during isochronal annealing was 0.1 K. Samples were mounted in a sample holder equipped with a chromel–alumel thermocouple for temperature control. The holder made it possible to quickly transfer samples into the oven and into liquid helium, and the cooling time to room temperature after each annealing was about 1–2 s.

To speed up diffusion processes, the studied materials were irradiated to a dose of 10^{-4} dpa (displacements per atom). The samples were irradiated with 5 MeV electrons in a LUE-5 linear electron accelerator in a flow cryostat in an atmosphere of purified helium. In this case, an electron beam scanning was used to achieve irradiation uniformity of about 10%. The irradiation temperature was maintained by temperature control of the flowing helium and changes in its flow rate, and amounted to 270 ± 10 K.

2.2. Theoretical Methods

The theoretical part of the work is to study the HEAs structure evolution by atomistic modeling methods. It should be noted that due to complex structure of HEAs (many components with high concentrations), this problem cannot be solved using MD methods. Indeed, the study of HEAs by classical molecular dynamics methods is very difficult, since the semiempirical interatomic interaction potentials used in this approach are not able to provide the necessary accuracy for the description of multicomponent systems. Quantum-mechanical calculations in the framework of the DFT theory are free of this drawback; however, they are computationally very expensive. As a result, DFT-based molecular dynamics can be used to simulate processes with duration no more than hundreds of picoseconds. Obviously, this is not enough for studying the diffusion-controlled evolution of the atomic structure of HEAs in an interesting temperature range from a practical point of view (300–1000 K). We use the iterative multiscale approach to overcome the described limitations. Its conceptual scheme is presented in Fig. 1. As can be seen from the figure, this scheme includes four main stages.

1. At the first stage, DFT calculations are performed for a large number of representative HEA structures, and the results are combined into a database.

2. At the next step, on the basis of the quantum-mechanical calculation base, the machine-learning multicomponent potential on the lattice (LRP) is parameterized.

3. Next, the obtained potential is used to model the atomic structure evolution of HEAs using atomistic MC method.

4. Based on simulation results, the most representative configurations of HEAs are chosen. Then, the LRP error is determined for these HEAs with respect to the DFT calculation results. If the error exceeds 5 meV/atom, then the self-consistency cycle shown in Fig. 1 proceeds to the next round. Namely, the data base is to be supplemented with a new set of representative configurations, the training of the potential occurs using the updated base, etc.

The calculation parameters from Sections 1–3 are described in detail below in subsections 2.2.1, 2.2.2, and 2.2.3, respectively. In addition, methods used to characterize the atomic structure of HEAs are described in subsection 2.2.4.

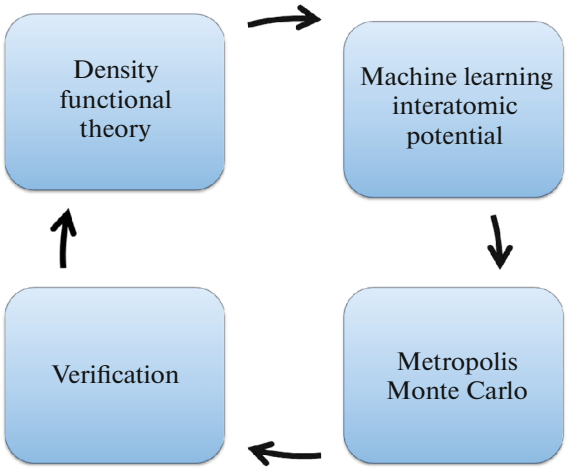

Fig. 1. Conceptual diagram of atomistic calculations of HEAs.

2.2.1. Quantum-mechanical calculations. Quantum-mechanical calculations were carried out in the framework of DFT using the Vienna Ab-Initio Simulation Package (VASP) computational code [51, 52]. The PAW pseudopotentials [53, 54] formulated in the generalized gradient approximation (PBE) [55] were employed in this work. For Fe, Cr, Ni, and Co pseudopotentials, the number of electrons outside the core was 8, 6, 10, and 9, respectively.

The initial coordinates of atoms were set in accordance with the positions of the sites of the fcc cubic lattice. The computational cell was a $2 \times 2 \times 2$ cube of the lattice period and, thus, contained 32 atoms. The cutoff energy of the plane wave basis was 350 eV. For integration by the Brillouin zone, a $3 \times 3 \times 3$ mesh was used. Plotting the mesh in reciprocal space was carried out using the Monkhorst–Pack method [56]. Using these parameters enabled achieving convergence in absolute value of the configuration energy within 1 meV/atom.

After setting the initial conditions, the potential energy of the system was minimized by the conjugate gradient method. The positions of the ions and the volume of the calculation cell underwent relaxation during the calculation. Magnetic degrees of freedom were not taken into account, since the Curie point of the alloy under study lies much lower than room temperature (about 130 K) [57].

The results of calculations of configurations representing a disordered solid solution were used as the initial database. That is, the choice of a chemical element (Fe, Co, Ni, or Cr), which would occupy a certain lattice site, was made randomly. In this case, the concentration of each element in the calculation cell could vary from 6 to 90 at %. Thus, a database of 1000 configurations was created, which was then iteratively supplemented in accordance with the scheme shown in Fig. 1.

2.2.2. Low-ranking interaction potential. To model the atomic structure evolution, it is necessary to describe the dependence of the energy of the system on the configuration of atomic surroundings. In this work, for this purpose, the low-rank interatomic interaction potential on the lattice was used (denoted above as LRP) [48]. LRP belongs to the class of machine-learning potentials; its main aim is to interpolate the results of quantum-mechanical calculations. Like other interatomic interaction potentials, LRP uses a number of assumptions. First, it is assumed that the total energy of the system (E_{total}) is representable as the sum of the contributions of individual configurations of surrounding atoms (E_i)

$$E_{\text{total}} = \sum_{i=1}^{N} E_i, \tag{1}$$

where N is the number of atoms in the system. Further, it is assumed that the atoms of the system are not strongly displaced relative to the sites of an ideal lattice. "Not strongly" means that all atoms of the system have the same number of nearest neighbors, 12 in the case of the fcc lattice under consideration. Then the contribution of the i-th atomic configuration to the energy of the system is uniquely determined by the set of types (Fe, Cr, etc.) of the nearest neighbors of the ith atom and its type. In other words,

$$E_i = V(\sigma_1 \ldots \sigma_n), \tag{2}$$

where $\sigma_1 \ldots \sigma_n$ is the set of parameters, characterizing the type of i-th atom and its nearest neighbors ($n = 13$ for fcc lattice); $V(\sigma_1 \ldots \sigma_n)$ is the interatomic interaction potential. In addition, it is assumed that with sufficient accuracy $V(\sigma_1 \ldots \sigma_n)$ is represented as the product of low-rank tensors. Therefore, V has the following form

$$V(\sigma_1 \ldots \sigma_n) = \prod_{i=1}^{n} A^{(i)}(\sigma_i), \tag{3}$$

where $A^{(i)}(\sigma_i)$ is the matrix of size $r_{i-1} \times r_i$, and $r_0 = r_n = 1$. In our work, r_1 and r_{n-1} were equal to 4, and $r_i = 8$ for others. The elements of matrices $A^{(i)}(\sigma_i)$ were determined by minimizing the mean square error

$$\frac{1}{K} \sum_{k=1}^{K} \left| E(\theta^{(k)}) - E^{\text{DFT}}(\theta^{(k)}) \right|^2, \tag{4}$$

where K is the number of configurations in the learning set, $\theta^{(k)}$ is the k-th configuration, $E(\theta^{(k)})$ and $E^{\text{DFT}}(\theta^{(k)})$ are the energies of the relevant configuration calculated using LRP and DFT, correspondingly.

2.2.3. Atomistic Monte Carlo. To simulate the structure evolution of HEAs, we used atomistic Monte Carlo method on lattice implemented in the

Table 1. Concentrations of chemical elements in the studied volume of CoCrFeNiMn

Element	Fe	Ni	Cr	Mn	Co	C	Si
at %	23.1 ± 0.2	18.9 ± 0.2	19.8 ± 0.2	18.6 ± 0.2	19.5 ± 0.2	0.73 ± 0.03	0.11 ± 0.03

SPPARKS software package [58]. The sequence of system configurations was generated using the algorithm by Metropolis [59]. The energy of each configuration was calculated using LRP, trained on the current database of quantum-mechanical calculations.

HEAs were simulated in a cubic computational cell with an edge length of 20 lattice periods. Thus, the cell contained 32000 atoms located at the sites of the fcc lattice. It should be noted that the computational efficiency of MC allows one to simulate systems of larger size. However, additional tests showed that for the considered systems this is impractical since the calculations using larger cells give the same result.

2.2.4. Nearest-order parameter and heat capacity. For quantitative analysis of the degree of ordering of the system under consideration, the Warren–Cowley short-range order (SRO) parameter [60] was used. For a binary composition, the order parameter α_{A-B} is determined according to the formula

$$\alpha_{A-B} = 1 - \frac{P_{AB}}{c_B}, \quad (5)$$

where P_{AB} is the conditional probability of the presence of atom B among the nearest neighbors of atom A, c_B is the concentration of atoms B in the calculation cell.

The correlation between parameter SRO and the local distribution of atoms can be illustrated by the following examples. If an atom of type A is predominantly surrounded by atoms of the same type, then probability P_{AB} is close to zero, and SRO is close to unity. If atoms of type A and B are randomly distributed in the computational cell, then P_{AB} is close to c_B, and SRO is close to zero. If an atom of type A is mainly surrounded by atoms of type B, then SRO has a negative value. The order parameter in formula (5) is defined for a pair of elements of type A and B. Therefore, an alloy with N components is characterized by the set of $\frac{N(N-1)}{2}$ order parameters. Similarly to the binary compound case described above, the order parameter α_{A-B} characterizes the distribution of type A and B atoms in a multicomponent system.

It should be noted that parameter SRO is convenient for describing the processes of local ordering, but it does not always permit accurately determining the temperature of the phase transition. For this purpose, it is much more convenient to use integral parameters characterizing the state of the system as a whole. One of these parameters is the specific heat capacity determined from the dispersion in the energy fluctuations of the system in the state of thermodynamic equilibrium. The formula for calculating the specific heat capacity is given by

$$C_p(T) = \frac{\langle E_i^2 \rangle - \langle E_i \rangle^2}{kT^2}, \quad (6)$$

where E_i is the energy of i-th configuration; k is the Boltzmann constant; T is the temperature. Angular brackets denote averaging over i, which is performed after the system is passed into the state of equilibrium.

3. RESULTS AND DISCUSSION

A discussion of the results obtained in the work is organized as follows. Firstly, we describe the results of the atomic-probe tomographic study of the initial structure of the samples. After that, the measured annealing curves of electrical resistivity are discussed. The last part of the section is devoted to a discussion of the results of modeling and interpretation of experimental data.

3.1. Analysis of the Initial State of the Samples

The Table 1 shows the chemical composition of the CoCrFeMnNi sample, which was studied using APT. According to the obtained data, the concentrations of various components differ by a few atomic percent. In particular, the concentration of chromium and iron in the sample is higher than equiatomic concentration, while the concentrations of nickel, manganese, and cobalt are lower. The total content of carbon and silicon is about 2%. The effect of these impurities on the results of experimental studies is not considered in this paper.

To characterize the initial state of the alloy, elemental distributions in the test sample were obtained according to the procedure described in Subsection 2.1.2. Atomic maps of the main elements of the alloy are shown in Fig. 2. The data presented indicate the absence of precipitation or segregation of the components. Thus, the initial state of the alloy is a solid solution without visually observed inhomogeneities.

However, local ordering of elements may occur in the alloy. To reveal it, a quantitative analysis of the distribution of the main components of the alloy relative to each other was carried out. In particular, probabilities of various concentrations of iron, nickel and chromium atoms were determined in the nearest surrounding of chromium atoms. For this purpose, a sphere with a radius of 2 nm was plotted around each chromium atom, and the concentration of the second ele-

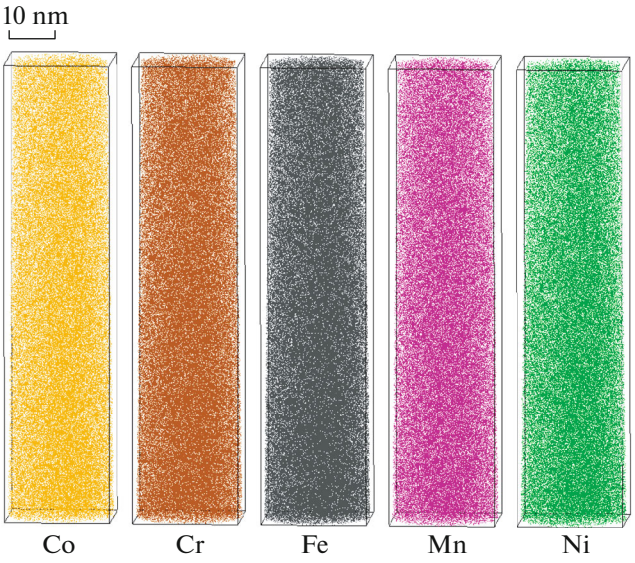

Fig. 2. Atomic maps of CoCrFeNiMn alloy in the original state.

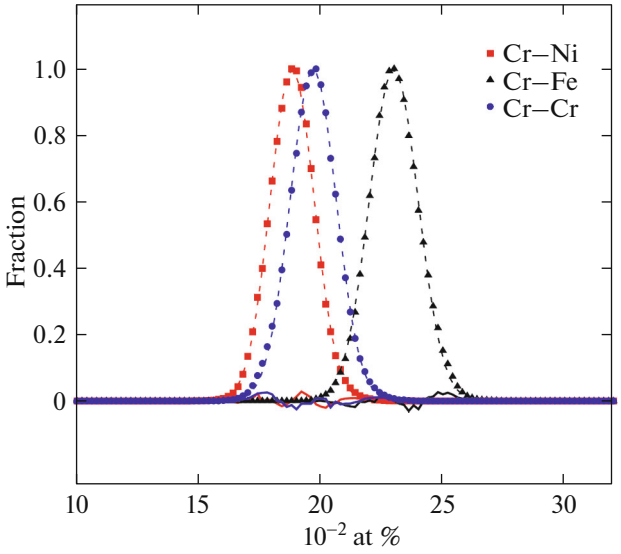

Fig. 3. Dependence of the fraction of Ni atoms (squares), Fe (triangles), and Cr (circles) from their concentration in a sphere of radius 2 nm around chromium atoms. Dotted lines: parameterization of experimental points of the normal distribution function; solid lines: difference between experimental data and the parameterized distribution function.

ment (iron, chromium, or nickel) in this sphere was calculated. For various values of the concentration of the second component, the fraction of chromium atoms around which this value of the concentration of the second component in the nearest environment was determined. In a disordered solid solution, this dependence has the form of a normal distribution, the center of which coincides with the concentration of the second component in the sample. The deviation of the obtained curve from the normal distribution indicates the presence of local inhomogeneities in the short-range order of atoms.

Figure 3 shows the relative concentrations of various atoms: Ni (squares), Fe (triangles), and Cr (circles). Dotted lines indicate data parameterization using the Gauss function. The solid lines at the bottom of the graph show the difference between the experimental data and the results of the curve parameterization. From the presented data it follows that the distributions under study are close to the normal distribution. This means that in the volume under study there is no ordering of elements and the formation of precipitates is absent. Thus, the initial state of CoCrFeNiMn is a disordered solid solution.

3.2. Electrical Resistivity of the Sample

An investigation of the atomic structure evolution of HEAs was carried out by measuring the temperature dependence of the residual electrical resistance during isochronal annealing. Figure 4 presents the results obtained for irradiated (dark symbols) and unirradiated (light symbols) CoCrFeNiMn (1), CoCrFeNi (2), and CrFeNiMn (3) samples. From the data presented we can conclude that temperature dependence of the electrical resistance of irradiated and unirradiated samples is significantly different. In particular, for unirradiated samples, a noticeable change in electrical resistance does not occur up to 550 K. After this, an almost linear increase in electrical resistance occurs, which reaches a maximum at 750–770 K. A further increase in temperature leads to a sharp drop in electrical resistance.

For irradiated samples, the temperature profile of electrical resistance is different from that described above. For these samples, the increase in electrical resistance starts at temperatures above 350 K. Similarly to unirradiated samples, an increase in electrical resistance is observed, reaching a certain constant value at 550 K (for CoCrFeNiMn and CoCrFeNi). With increasing temperature to 750 K, the electrical resistance of these samples practically does not change. A further increase in temperature above 770 K leads to a sharp drop in electrical resistance, as for unirradiated samples. We can see that for each alloy that above 800 K the graphs merge into a single dependence for irradiated and unirradiated samples. This points to the equilibrium character of this dependence, determined by the annealing temperature and caused by thermal diffusion.

It should be noted that with a specific residual electrical resistance of irradiated samples at a level of 100 μΩ/cm, the magnitude of the observed growth is about two orders of magnitude higher than the expected increase in electrical resistance due to the accumulation of radiation defects. Thus, the described

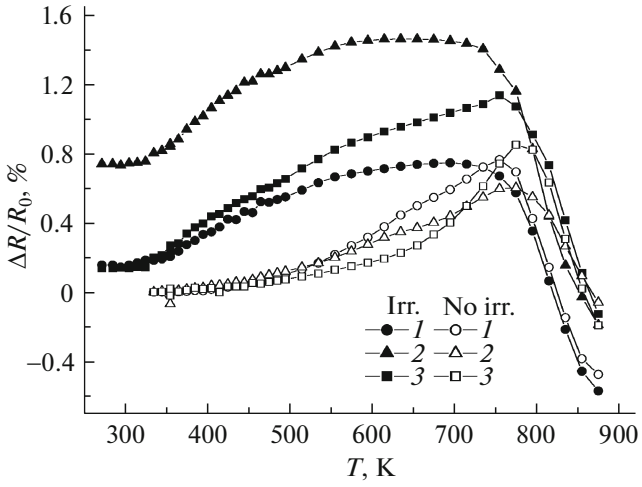

Fig. 4. Temperature dependence of the relative change in electrical resistance for CoCrFeNiMn samples (*1*), CoCrFeNi (*2*) and CrFeNiMn (*3*). Irradiated samples are indicated by dark symbols; nonirradiated, by light ones.

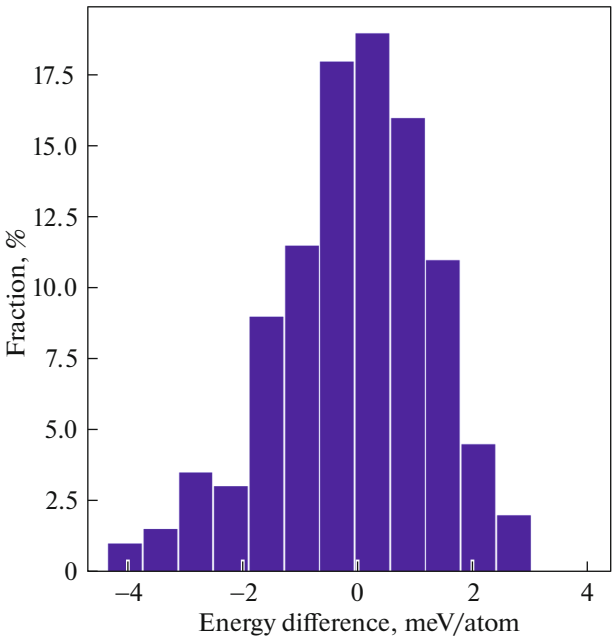

Fig. 5. Histogram distribution of the potential energy errors calculated using LRP, rms error is 1.4 meV/atom.

increase in electrical resistance cannot be explained by the accumulation of radiation defects during irradiation.

The above described behavior of the electrical resistance can be explained by diffusion-controlled formation of precipitates that decay at a temperature of 770 K. The difference in the electrical resistance profile for irradiated and nonirradiated samples is due to the acceleration of diffusion processes, which is caused by the migration of vacancies formed during electron irradiation of alloys. This leads to an accelerated formation of precipitates in irradiated samples compared with unirradiated ones. The resulting precipitates are thermodynamically stable up to 770 K. Therefore, the electrical resistance is practically unchanged at temperatures from 550 to 770 K. The precipitates dissolve at higher temperatures, significantly reducing the electrical resistance. Thus, the results manifest that in the considered multicomponent materials the precipitate formation may occur at temperatures up to 770 K. However, these data, as well as the APT results, do not allow us to determine the composition of these precipitates.

3.3. Calculation Results

To determine the composition of precipitates formed during isochronal annealing in Subsection 3.2, we studied the thermodynamic stability of the CoCrFeNi system. For this system, as for CoCrFeMnNi, similar trends are observed. However, CoCrFeNi has a simpler chemical composition, which simplifies the solution of this problem. The description of the results of theoretical studies in the next section is organized as follows. The verification results of the used on-lattice potential are given in the first part. Thermodynamically equilibrium structures in CCFN over a wide temperature range are described further. Finally, the results of the calculations are presented in which the atomic structure evolution of CCFN during isochronal annealing was studied to reproduce the results of measuring the electrical resistance.

3.3.1. Comparison of DFT and LRP. To verify the potential used, a comparison was made of the potential energies obtained using DFT and LRP for configurations from the test set. In these configurations, the atoms of various types have random arrangement by the crystal lattice sites. In addition, these configurations were not used to obtain the potential on the lattice. The histogram of the LRP error distribution relative to the DFT is shown in Fig. 5. According to the data presented, the error distribution is close to normal with a standard error of 1.4 meV/atom. This error is close to the accuracy of calculating the potential energy by the DFT method. So the used low-ranking interatomic interaction potential reproduces the potential energy values for various configurations with an accuracy close to the DFT accuracy.

3.3.2. Equilibrium CCFN structures. In order to study the boundaries of the single-phase existence of CCFN, a series of Monte Carlo calculations was carried out in temperature range from 373 to 1600 K. For each temperature, the initial state of the system was a disordered solid solution. At least 10^4 jumps per atom performed in the computational cell before reaching the thermodynamic equilibrium of the system. An analysis of the atomic structure of the final states of

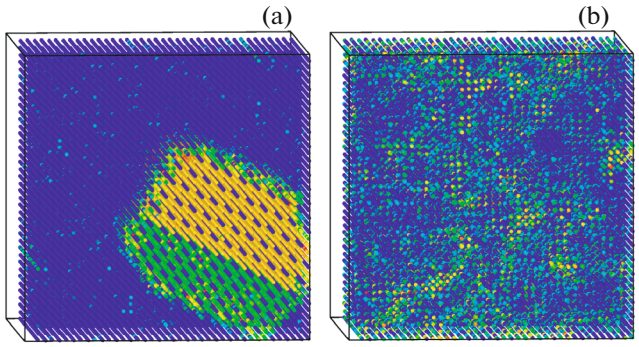

Fig. 6. Formation of the Ni_2Cr and Ni_4Cr precipitates (light and dark symbols, respectively) at 500 K (a), and disordered solid solution at 950 K (b).

the system showed that the formation of two ordered structures occurs in CCFN. First, at temperatures up to 1000 K, a simple cubic lattice of chromium atoms is formed. This means that chromium atoms in the sublattice do not have other chromium atoms among their nearest neighbors. Second, Ni–Cr precipitates are formed at temperatures below 850 K. The composition of these precipitates changes with temperature: below 600 K, they consist of a mixture of Ni_2Cr and Ni_4Cr, and between 600 and 850 K, they consist of Ni_4Cr. As an example, Fig. 6a shows a mixture of Ni_2Cr (dark region) and Ni_4Cr (bright region) of these precipitates at a temperature of 500 K.

To illustrate the behavior of HEAs at higher temperatures, Fig. 6b shows the formation of a disordered solid solution at a temperature of 950 K.

In order to check the results described above, additional DFT calculations were carried out, the purpose of which was to determine the enthalpy of the Ni_4Cr precipitate formation. To calculate the enthalpy, the decomposition reaction of a disordered CCFN solid solution into a mixture of Ni_4Cr precipitate (*i*) and a system with chromium sublattice (*ii*) was considered. The potential energy for (*i*) and (*ii*) was determined by averaging the energies for 10 different configurations. According to the results, the enthalpy of formation of Ni_4Cr precipitate is −27 meV/atom in the DFT calculations and −36 meV/atom in the LRP calculations. It should be noted that the formation of Ni–Cr precipitates was also observed in other works [61, 62]. In the above studies, it was shown that precipitates based on Ni_2Cr are formed at temperatures up to 800 K. Thus, the performed DFT calculations confirm the formation of Ni–Cr precipitates in CCFN at low temperatures being consistent with the results published in other works. To determine the decay temperature of ordered structures (Ni–Cr precipitates and chromium sublattices) more accurately using formula (6), we calculated the specific heat capacity of the system in the considered temperature range. Its temperature dependence is shown in Fig. 7. The graph shows two distinct peaks of specific heat capacity corresponding to the decay of the ordered structures at 773 and 973 K. An analysis of the atomic structure of the corresponding configurations showed that Ni–Cr precipitates decay at 773 K, while the cubic chromium sublattice decays at 973 K.

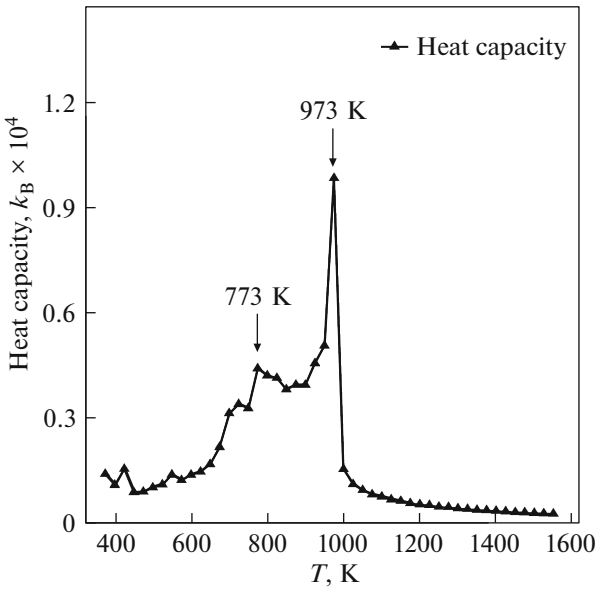

Fig. 7. Temperature dependence of specific heat capacity C_p.

3.3.3. Concentration of precipitates at isochronal annealing. As was shown above, for the initial state of CoCrFeMnNi, the distribution of element concentrations around chromium atoms differs from the normal one. This deviation may be due to the initial stage of precipitate formation. This assumption is confirmed by the results of measurements of electrical resistance during isochronal annealing. Indeed, with an increase in temperature to 770 K, an increase in electrical resistance is observed for three samples of HEAs. This increase may be associated with an increase in the concentration of precipitates. However, the composition of these precipitates cannot be determined from the data presented. To resolve this issue, a series of additional calculations was performed to reproduce the results of measurements of electrical resistance.

In preparation for calculations, for each temperature, at which the electrical resistance was determined, the number of jumps per atom occurred in the system during measurement was obtained. This number was calculated by the formula

$$N_{\text{jumps}} = \frac{6Dt_{\text{anneal}}}{\Delta^2}, \quad (7)$$

where N_{jumps} is the number of jumps per atom during annealing time t_{anneal}, D is the self-diffusion coefficient of atoms, Δ is the distance between the nearest neigh-

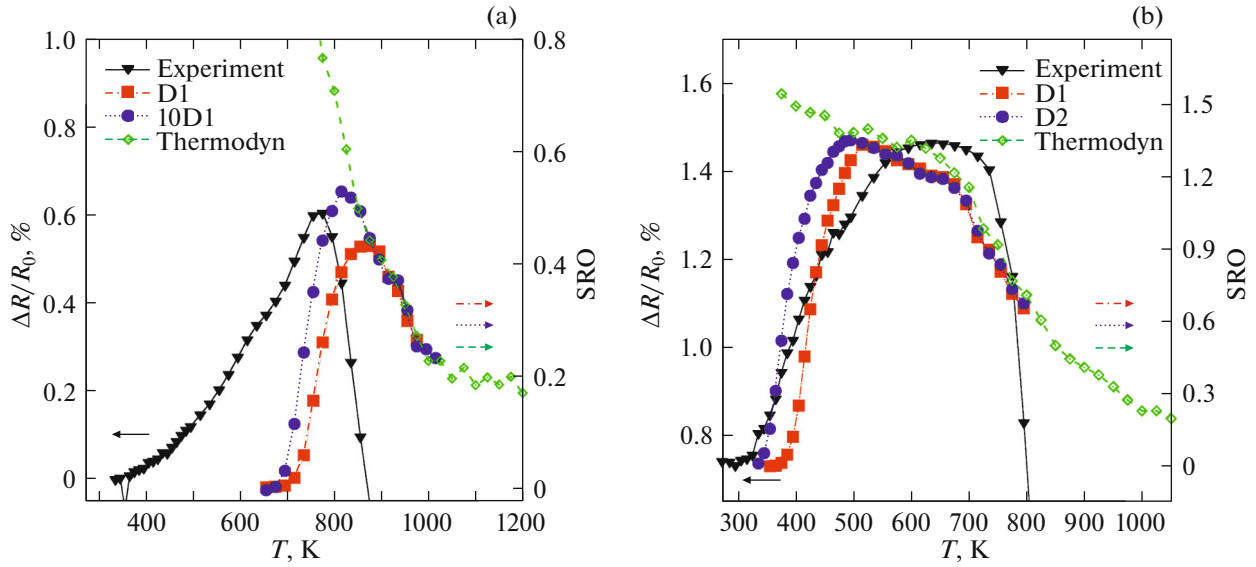

Fig. 8. Temperature dependence of the change in electrical resistance and order parameter for Ni atoms for unirradiated (a) and irradiated (b) sample. Solid line (triangles): experimental values of electrical resistance; dashed-dotted line (squares): the order parameter for calculations with diffusion coefficient from [63]; dashed line: accelerated diffusion; dashed line (rhombs): thermodynamically equilibrium parameter of order.

bors. To calculate the self-diffusion coefficient, the experimentally determined parameters were used (preexponential factor and activation energy) [63]. A disordered solid solution was the initial state of the system. After that, the calculation was performed for each temperature until the required number of jumps per atom was accumulated. The final state of the system was taken as the initial one for the next calculation at a higher temperature. Negative-order parameter $-\alpha_{Ni-Ni}$ for nickel atoms was used for a numerical estimate of the degree of ordering.

Figure 8a shows the calculation results. As expected, the diffusion processes are slowed down at low temperatures and the system under study does not have time to reach thermodynamic equilibrium. Therefore, at low temperatures, the red curve is lower than the thermodynamically equilibrium one. With increasing temperature, these curves will approach each other. At a certain temperature, the order parameters in both calculations become the same.

According to the presented data, the curves of the temperature dependence of the electrical resistance and the order parameter have a similar profile. Nevertheless, the maximum change in electrical resistance occurs at 753 K, while the order parameter reaches a maximum at 853 K. Also, a noticeable increase in the electrical resistance begins at 450 K, although $-\alpha_{Ni-Ni}$ begins to grow at 730 K. This means that the temperature dependence of the order parameter is shifted to higher temperatures by more than 100 K.

An analysis of the atomic structure showed that an increase in the order parameter is associated with the formation of Ni_2Cr and Ni_4Cr precipitates at temperatures up to 850 K. An increase in the concentration of precipitates is consistent with an increase in electrical resistance. However, to explain the temperature shift of the order parameter curve in comparison with the electrical resistance curve, it is necessary to perform additional calculations. Significant difference between experimental and calculated data is likely caused by the following. To determine the number of jumps per atom that occurs at each temperature during isochronal annealing, we used experimentally determined self-diffusion coefficients [63]. This approach assumes a constant value of the vacancy migration energy. However, in multicomponent systems, this value quantity depends on the local environment of the diffusing atom. Therefore, the rate of self-diffusion can vary greatly in disordered solid solution and in precipitate. This difference can lead to a significant difference in the number of jumps per atom in the experiment compared to that calculated using the experimental self-diffusion coefficient.

To verify this assumption, additional calculations were performed in which the self-diffusion coefficient in CCFN and, accordingly, the number of jumps per atom were increased by 10 times. In Fig. 8a these results are shown by circles. According to the data obtained, the temperature at which the maximum of the order parameter $-\alpha_{Ni-Ni}$ is reached decreased by 40 K. Thus, the kinetics of precipitate formation in the calculations strongly depends on the rate of diffusion processes. Therefore, in order to achieve better agreement with experimental data, it is necessary to take into account the dependence of the migration energy

on the local surrounding. To study the formation of ordered structures in irradiated samples, similar calculations were performed. In these calculations, the contribution to diffusion from vacancies formed during electron irradiation was taken into account:

$$D_{\text{irrad}} = D_{\text{thermal}} + fD_V c_V, \quad (8)$$

where D_{thermal} is the thermal self-diffusion coefficient, which was used above, f is the correlation factor, D_V and c_V are the diffusion coefficient and concentration of vacancies in an irradiated sample, respectively. The vacancy diffusion coefficient was calculated from the self-diffusion coefficients published in [63, 64]. In [65], the enthalpy of vacancy formation was determined as the arithmetic mean of the vacancy formation enthalpy for each element (Co, Cr, Fe, and Ni).

Figure 8b shows the calculation results. We can see from the figure that for the irradiated sample, a noticeable growth in electrical resistance (triangles) starts at 330 K and reaches a maximum at 600 K. With increasing temperature, the electrical resistance remains constant up to 730 K, at higher temperatures the electrical resistance decreases. In calculations performed using the self-diffusion coefficient from [64] (circles) and [63] (squares), a noticeable increase in the order parameter occurs at 350 and 400 K, respectively. In both calculations, the maximum value of the order parameter is reached at 500 K. This means that the formation of precipitates in the experiments occurs in a wider temperature range than in the calculations. Nevertheless, the performed calculations predict with high accuracy the characteristic formation temperatures of the Ni–Cr precipitates.

At temperatures above 500 K, more than 10^6 jumps per atom occur in the system. This is sufficient to achieve the state of thermodynamic equilibrium in the system. Therefore, the order parameter will correspond to a thermodynamically equilibrium value (rhombs) at temperatures above 500 K. As we can see in the graph, the order parameter is a slowly decreasing function at temperatures from 600 to 1000 K. This means that, according to the calculations, Ni_4Cr precipitates gradually dissolve in this temperature range. Using these results, it is possible to determine only the characteristic temperature of dissolution of the precipitates. We assume that at this temperature the order parameter has the average value between the maximum and minimum ones $-\alpha_{\text{Ni–Ni}}$, which is reached in this temperature range. Thus, the characteristic decay temperature of the Ni_4Cr precipitates is about 800 K.

On the other hand, from experimental data it follows that the dissolution of precipitates takes place in a narrow temperature range. This can be seen from the drastic drop in electrical resistance at 770 K. Thus, the characteristic dissolution temperature of the Ni_4Cr precipitates in the calculations is close to the experimental temperature of the electrical resistance drop. However, in the calculations, the dissolution of precipitates occurs in a wider temperature range than in the experiment.

4. CONCLUSIONS

In this work, we studied the processes of formation of secondary phase precipitates in high-entropy alloys based on Co, Cr, Fe, Ni, and Mn. The experimental part of the work includes studies of the alloy microstructure by atom probe tomography (APT), as well as measurements of isochronal annealing curves of residual electrical resistance. The theoretical part of the study involves multiscale modeling of evolution of the CoCrFeNi atomic structure. For this purpose, a database of the results of quantum mechanical calculations was created. On this basis, the low-ranking interatomic interaction potential was parametrized, which was then used in the calculations by the Monte Carlo–Metropolis method.

The analysis of the initial state of the CoCrFeMnNi system performed using APT did not reveal visually detectable precipitates. However, an increase in electrical resistance during isochronal annealing indicates the formation of electron scattering centers at temperatures up to 770 K. The results of theoretical studies showed the formation of Ni_2Cr and Ni_4Cr precipitates in the CoCrFeNi system decaying at 600 and 800 K, respectively.

The calculations also made it possible to reproduce dependence of electrical resistance during isochronal annealing. For the irradiated sample, the characteristic formation and decay temperatures of precipitates determined in the calculations are close to experimental values. For the unirradiated sample, calculations predict a higher precipitate formation temperature than that observed in the experiment. This difference can be caused by the dependence of the vacancy migration barrier on the local surrounding, which was not accounted for in this work.

Thus, in this work, we developed a calculation technique that enables performing multiscale modeling of multicomponent systems on experimentally achievable spatial and temporal scales. This technique was verified on the CoCrFeNi high-entropy alloy. The calculation results were shown to agree with experimental data.

FUNDING

The work was supported by the Russian Science Foundation, project no. 18-32-00736. Tomographic atom probe analysis was performed using the equipment of the CAMICS Collective Use Center (http://kamiks.itep.ru/) in SRC Kurchatov Institute—ITEP.

CONFLICT OF INTEREST

The authors declare that they have no conflicts of interest.

REFERENCES

1. J.-W. Yeh, S.-K. Chen, S.-J. Lin, J.-Y. Gan, T.-S. Chin, T.-T. Shun, C.-H. Tsau, and S.-Y. Chang, Adv. Eng. Mater. **6**, 299 (2004).
2. B. Cantor, I. T. H. Chang, P. Knight, and A. J. B. Vincent, Mater. Sci. Eng. A **375–377**, 213 (2004).
3. D. B. Miracle and O. N. Senkov, Acta Mater. **122**, 448 (2017).
4. E. J. Pickering and N. G. Jones, Int. Mater. Rev. **61**, 183 (2016).
5. F. Otto, Y. Yang, H. Bei, and E. P. George, Acta Mater. **61**, 2628 (2013).
6. O. N. Senkov, J. D. Miller, D. B. Miracle, and C. Woodward, CALPHAD **50**, 32 (2015).
7. M. C. Troparevsky, J. R. Morris, R. Paul, C. Kent, A. R. Lupini, and G. M. Stocks, Phys. Rev. X **5**, 011041 (2015).
8. O. N. Senkov and D. B. Miracle, J. Alloys Compd. **658**, 603 (2016).
9. Y. F. Ye, J. Wang, J. Lu, C. T. Liu, and Y. Yang, Scr. Mater. **104**, 53 (2015).
10. I. Toda-Caraballo and P. E. J. Rivera-Díaz del Castillo, Intermetallics **71**, 76 (2016).
11. D. J. M. King, S. C. Middleburgh, A. G. McGregor, and M. B. Cortie, Acta Mater. **104**, 172 (2016).
12. Z. Leong, J. S. Wróbel, S. L. Dudarev, R. Goodall, I. Todd, and D. Nguyen-Manh, Sci. Rep. **7**, 39803 (2017).
13. N. Yurchenko, N. Stepanov, and G. Salishchev, Mater. Sci. Technol. **33**, 17 (2017).
14. Ming-Hung Tsai, Jian-Hong Li, An-Chen Fan, and Pei-Hua Tsai, Scr. Mater. **127**, 6 (2017).
15. G. A. Salishchev, M. A. Tikhonovsky, D. G. Shaysultanov, N. D. Stepanov, A. V. Kuznetsov, I. V. Kolodiy, A. S. Tortika, and O. N. Senkov, J. Alloys Compd. **591**, 11 (2014).
16. A. Gali and E. P. George, Intermetallics **39**, 74 (2013).
17. Minju Kang, Jong Woo Won, Jun Beom Kwon, and Young Sang Na, Mater. Sci. Eng. A **707**, 16 (2017).
18. B. Gludovatz, A. Hohenwarter, D. Catoor, E. H. Chang, E. P. George, and R. O. Ritchie, Science (Washington, DC, U. S.) **345**, 1153 (2014).
19. A. J. Zaddach, C. Niu, C. C. Koch, and D. L. Irving, J. Mater. **65**, 1780 (2013).
20. O. N. Senkov, G. B. Wilks, J. M. Scott, and D. B. Miracle, Intermetallics **19**, 698 (2011).
21. M. A. Hemphill, T. Yuan, G. Y. Wang, J. W. Yeh, C. W. Tsai, A. Chuang, and P. K. Liaw, Acta Mater. **60**, 5723 (2012).
22. M.-H. Chuang, M. H. Tsai, W.-R. Wang, S.-J. Lin, and J.-W. Yeh, Acta Mater. **59**, 6308 (2011).
23. Ch. Lu, L. Niu, N. Chen, K. Jin, T. Yang, P. Xiu, Y. Zhang, F. Gao, H. Bei, Sh. Shi, M.-R. He, I. M. Robertson, W. J. Weber, and L. Wang, Nat. Commun. **7**, 13564EP (2016).
24. K. Jin, C. Lu, L. M. Wang, J. Qu, W. J. Weber, Y. Zhang, and H. Bei, Scr. Mater. **119**, 65 (2016).
25. C. Hofer, E. Stergar, S. A. Maloy, Y. Q. Wang, and P. Hosemann, J. Nucl. Mater. **458**, 361 (2015).
26. Ch. Lu, T. Yang, K. Jin, N. Gao, P. Xiu, Y. Zhang, F. Gao, H. Bei, W. J. Weber, K. Sun, Y. Dong, and L. Wang, Acta Mater. **127**, 98 (2017).
27. M. S. Lucas, G. B. Wilks, L. Mauger, J. A. Muñoz, O. N. Senkov, E. Michel, J. Horwath, S. L. Semiatin, M. B. Stone, D. L. Abernathy, and E. Karapetrova, Appl. Phys. Lett. **100**, 251907 (2012).
28. K. A. Christofidou, E. J. Pickering, P. Orsatti, P. M. Mignanelli, T. J. A. Slater, H. J. Stone, and N. G. Jones, Intermetallics **92**, 84 (2018).
29. U. Dahlborg, J. Cornide, M. Calvo-Dahlborg, T. C. Hansen, A. Fitch, Z. Leong, S. Chambreland, and R. Goodall, J. Alloys Compd. **681**, 330 (2016).
30. C. Niu, A. J. Zaddach, A. A. Oni, X. Sang, J. W. Hurt III, J. M. LeBeau, C. C. Koch, and D. L. Irving, Appl. Phys. Lett. **10616**, 161906 (2015).
31. Y. Brif, M. Thomas, and I. Todd, Scr. Mater. **99**, 93 (2015).
32. F. He, Zh. Wang, Q. Wu, J. Li, J. Wang, and C. T. Liu, Scr. Mater. **126**, 15 (2017).
33. N. D. Stepanov, D. G. Shaysultanov, M. S. Ozerov, S. V. Zherebtsov, and G. A. Salishchev, Mater. Lett. **185**, 1 (2016).
34. M. V. Klimova, D. G. Shaysultanov, R. S. Chernichenko, V. N. Sanin, N. D. Stepanov, S. V. Zherebtsov, and A. N. Belyakov, Mater. Sci. Eng. A **740–741**, 201 (2019).
35. D. Choudhuri, S. Shukla, W. B. Green, B. Gwalani, V. Ageh, R. Banerjee, and R. S. Mishra, Mater. Res. Lett. **6**, 171 (2018).
36. Chuan Zhang, Fan Zhang, Shuanglin Chen, and Weisheng Cao, J. Mater. **64**, 839 (2012).
37. Su-Wen Kao, Jien-Wei Yeh, and Tsung-Shune Chin, J. Phys.: Condens. Matter **20**, 145214 (2008).
38. G. Anand, R. Goodall, and C. L. Freeman, Scr. Mater. **124**, 90 (2016).
39. D. Ma, B. Grabowski, F. Dormann, J. Neugebauer, and D. Raabe, Acta Mater. **100**, 90 (2015).
40. L. J. Santodonato, Y. Zhang, M. Feygenson, C. M. Parish, M. C. Gao, R. J. Weber, J. C. Neuefeind, Z. Tang, and P. K. Liaw, Nat. Commun. **6**, 5964 (2015).
41. M. Gao and D. Alman, Entropy **15**, 4504 (2013).
42. A. Tamm, A. Aabloo, M. Klintenberg, M. Stocks, and A. Caro, Acta Mater. **99**, 307 (2015).
43. H. Heidsiek, R. Scheffel, and K. Lücke, J. Phys. Colloq. **38**, C7 (1977).
44. G. Antesberger, W. Kesternich, K. Sonnenberg, and B. D. Sharma, Rad. Effects **38**, 45 (1978).
45. K. L. Lücke, H. Haas, and H. A. Schulze, J. Phys. Chem. Solids **3711**, 979 (1976).
46. C. Dimitrov, M. Tenti, and O. Dimitrov, J. Phys. F **11**, 753 (1981).
47. S. E. Danilov, V. L. Arbuzov, and V. A. Kazantsev, J. Nucl. Mater. **414**, 200 (2011).
48. A. Shapeev, Comput. Mater. Sci. **139**, 26 (2017).
49. S. V. Rogozhkin, A. A. Aleev, A. A. Lukyanchuk, A. S. Shutov, O. A. Raznitsyn, and S. E. Kirillov, Instrum. Exp. Tech. **60**, 428 (2017).
50. J. M. Hyde, A. Cerezo, and T. J. Williams, Ultramicroscopy **109**, 502 (2009).

51. G. Kresse and J. Furthmüller, Phys. Rev. B **54**, 11169 (1996).
52. G. Kresse and J. Furthmüller, Comput. Mater. Sci. **6**, 15 (1996).
53. G. Kresse and D. Joubert, Phys. Rev. B **59**, 1758 (1999).
54. P. E. Blüchl, Phys. Rev. B **50**, 17953 (1994).
55. J. P. Perdew, K. Burke, and M. Ernzerhof, Phys. Rev. Lett. **77**, 3865 (1996).
56. H. J. Monkhorst and J. D. Pack, Phys. Rev. B **13**, 5188 (1976).
57. M. S. Lucas, D. Belyea, C. Bauer, N. Bryant, E. Michel, Z. Turgut, S. O. Leontsev, J. Horwath, S. L. Semiatin, M. E. McHenry, and C. W. Miller, J. Appl. Phys. **113**, 17A923 (2013).
58. A. Slepoy, A. P. Thompson, and S. J. Plimpton, J. Chem. Phys. **128**, 205101 (2008).
59. N. Metropolis, A. W. Rosenbluth, M. N. Rosenbluth, A. H. Teller, and E. Teller, J. Chem. Phys. **21**, 1087 (1953).
60. J. M. Cowley, Phys. Rev. **120**, 1648 (1960).
61. A. Marucco, Mater. Sci. Eng. A **189**, 267 (1994).
62. E. Lang, V. Lupinc, and A. Marucco, Mater. Sci. Eng. A **114**, 147 (1989).
63. K.-Y. Tsai, M.-H. Tsai, and J.-W. Yeh, Acta Mater. **61**, 4887 (2013).
64. M. Vaidya, S. Trubel, B. S. Murty, G. Wilde, and S. V. Divinski, J. Alloys Compd. **688**, 994 (2016).
65. Weiliang Chen, Xueyong Ding, Yuchao Feng, Xiongjun Liu, Kui Liu, Z. P. Lu, Dianzhong Li, Yiyi Li, C. T. Liu, and Xing-Qiu Chen, J. Mater. Sci. Technol. **34**, 355 (2018).

Translated by G. Dedkov